



TECHNICAL ARTICLE

# Hot Compression Behavior and Workability of Mg-5Gd-3Y-2Zn-0.5Zr Alloy with Long-Period Stacking Ordered Phases

Xiaodong Yang, Baolong Liu, Xiaojie Zhou, Weiyang Huang, Liwei Lu, Xianzheng Lu, and Yaru Liu

Submitted: 25 May 2022 / Revised: 17 June 2022 / Accepted: 29 June 2022 / Published online: 23 August 2022

The compression behavior and workability of the Mg-5Gd-3Y-2Zn-0.5Zr (designated as 2#) alloy with long-period stacking ordered (LPSO) phases were investigated and compared with those of the Mg-5Gd-3Y-1Zn-0.5Zr (designated as 1#) one. The results reveal that the increased volume fraction of interdendritic LPSO phases and the formation of thermostable intragranular lamellar LPSO phases can be induced by the increase in Zn content. The lamellar LPSO phases appear after homogenization and keep undissolved during compression, which strongly inhibit the dynamic recrystallization. The 2# alloy exhibits the deteriorated workability which is embodied in the larger deformation activation energy ( $Q$ ,  $\sim 336$  kJ/mol), lower DRX ratios, broader improper processing domains, and higher frequency of macrocracks. Moreover, the increased Zn content leads to the higher grain size exponent ( $m$ ,  $\sim 5.4$ ) due to the combined effects of increased interdendritic and intragranular LPSO phases for the 2# alloy. This work aims to provide useful information for the industrial production of Mg alloys which contain LPSO phases.

**Keywords** dynamic recrystallization, long-period stacking ordered, magnesium alloys, morphology, workability

## 1. Introduction

Magnesium alloys have been increasingly applied in the fields of load bearing, biodegradable implants, and energy storage due to their high specific strength (Ref 1-9), good biocompatibility (Ref 10-12), high hydrogen storage density (Ref 13-16), etc. As the structural materials, Mg-Gd-Y-Zn-Zr alloys with long-period stacking ordered (LPSO) phases exhibit outstanding mechanical properties and have drawn increasing attention in recent years (Ref 17-23). For instance, Xu et al. (Ref 17) prepared a high-strength Mg-8.2Gd-3.8Y-1.0Zn-0.4Zr (wt.%) alloy sheet by rolling and aging, with an ultimate tensile strength (UTS) of 517 MPa. After a series of thermal and mechanical treatments, Sun et al. (Ref 18) obtained a much higher hardness for this same Mg-8.2Gd-3.8Y-1.0Zn-0.4Zr alloy than other reported wrought Mg alloys. Moreover, an excellent strength-ductility synergy has also been achieved in the Mg-9.5Gd-4Y-2.2Zn-0.5Zr alloys by the pre-aging treat-

ment prior to extrusion or an alternating aging-annealing process after extrusion (Ref 20, 21). Therein, LPSO phases play a negligible role in enhancing the mechanical properties.

However, it was reported that the existence of LPSO phase would reduce the workability of Mg alloys (Ref 22, 24-29). The introduction of 18R-type LPSO phases into the Mg-2.0Zn-0.3Zr alloy by addition of 5.8wt.%Y element increased its deformation activation energy  $Q$  from 169.8 to 293.0 kJ/mol (Ref 24). Although the addition of Zn element into the Mg-12Gd-1Mn-0.5Zr alloy brought about LPSO phases to enhance the strength, these phases inhibited the dynamic recrystallization (DRX) behavior and narrowed the suitable deformation parameter zones in the dynamic materials model (DMM) processing maps (Ref 26). Under this condition, we previously fabricated a high-performance Mg-4.9Gd-3.2Y-1.1Zn-0.5Zr alloy by multidirectional forging (MDF) based on careful analysis of the compression behavior and processing maps so as to avoid macro structural defects during MDF (Ref 22). It seems urgent to study how to improve the workability of the Mg-Gd-Y-Zn-Zr alloys without avoiding the existence of LPSO phases.

The modifying of LPSO phases mainly involves two aspects, structure and morphology (Ref 27). Among different stacking sequences of LPSO phases (such as 6H, 10H, 14H, 18R, and 24R), 18R and 14H structures are the most common ones (Ref 5, 30, 31). Therein, 14H structure is more thermal stable after annealing treatment (Ref 31, 32). Considering that Mg alloys are usually homogenized before plastic deformation, the structure of LPSO phases might be fixed as 14H in this case. Nevertheless, the structural change from 18R into 14H was demonstrated to increase the  $Q$ , delay the DRX, and eventually reduce the workability (Ref 25). Instead, it is more feasible to modify the LPSO morphology which involves the volume fraction, distribution (interdendritic or intragranular), and shape (block, thin-platelet, lamellar, etc.) (Ref 27). As a

Xiaodong Yang, Xiaojie Zhou, Weiyang Huang, Xianzheng Lu, and Yaru Liu, Hunan Provincial Key Laboratory of Intelligent Manufacturing Technology for High-Performance Mechanical Equipment, Changsha University of Science and Technology, Changsha 410114, China; Baolong Liu, Beijing Institute of Remote Sensing Equipment, Beijing 100854, China; Liwei Lu, Hunan Provincial Key Laboratory of High Efficiency and Precision Machining of Difficult-to-Cut Material, Hunan University of Science and Technology, Xiangtan 411201, China. Contact e-mails: xjzhoucsu@163.com and huangwy@csust.edu.cn.

key element to form LPSO phase in Mg-RE alloys, the effects of Zn content on the mechanical properties, aging-strengthening response, precipitation sequence, etc., were systematically studied (Ref 33-38). However, the effect of LPSO morphology (changed by the Zn content) on the related DRX behavior,  $Q$  value and workability also deserves investigation.

In this work, a Mg-5Gd-3Y-2Zn-0.5Zr alloy was investigated in comparison with our previously reported Mg-5Gd-3Y-1Zn-0.5Zr one (Ref 22), in the aspects of LPSO morphology, deformation behavior (e.g., flow stress, activation energy, DRX behavior), DMM processing maps, etc. By understanding the effect of LPSO morphology on the compression behavior and workability, this work aims to provide guidance for the industrial production of LPSO-containing Mg alloys.

## 2. Experimental Procedures

The studied alloy was prepared by melting pure Mg and Zn, Mg-25Gd, Mg-25Y, Mg-25Zr (wt.%) master alloys in an electrical resistance furnace and then pouring into a water-cooling iron mold with an inner size of  $\Phi$  70 mm  $\times$  200 mm, under the protection of a mixed atmosphere of CO<sub>2</sub> and Ar. The actual composition (wt.%) was examined to be Mg-5.0Gd-3.1Y-2.1Zn-0.5Zr by an inductively coupled plasma (ICP, SPECTRO BLUE SOP) analyzer, with the incident frequency of 27 MHz and power of 1400 W. After homogenization at 510 °C for 24 h, specimens with the size of  $\Phi$  10mm  $\times$  15 mm for compression were cut from the center of the ingot.

To ensure the comparability of the results, the compression specimens of the 2# alloy were compressed with the same schedules on the same Gleeble-3500 thermomechanical simulator as reported in our previous work (Ref 22). The key parameters involve the compression temperature range of 350-500 °C, average strain rates ( $\dot{\epsilon}$ ) of 0.001-1 s<sup>-1</sup>, and true strain of 1.0. The main difference between the 1# and 2# alloy belongs to the Zn content, as listed in Table 1.

Microstructure at the central region of all compressed samples was characterized by a scanning electron microscope (SEM, Phenom G2) equipped with an energy-dispersive spectrometer (EDS). Before SEM observation, specimens were ground and polished, followed by etching in a solution of 6 g picric acid, 40 mL acetic acid, 40 mL water, and 100 mL ethanol. Electron back-scatter diffraction (EBSD) data were examined on a Helios Nanolab 600i SEM equipped with the HKL EBSD system, with a scanning step of 0.2  $\mu$ m. The EBSD samples were electron-polished at -40 °C in a solution of 15 mL perchloric acid and 285 mL ethyl alcohol. In order to qualitatively analyze and compare the microstructure, the size and volume fractions of the DRXed (dynamically recrystallized) grains and LPSO phases were measured by the Image-Pro Plus 6.0 software from SEM or EBSD maps of low

magnification. More than 300 grains were counted to ensure the statistical significance of the results.

## 3. Results

### 3.1 Microstructure of the 2# Homogenized Alloy

Figure 1 shows the SEM image of the 2# homogenized alloy. Coarse interdendritic LPSO phases locate at the boundaries of  $\alpha$ -Mg grains which are filled with intragranular lamellar LPSO phases. Interdendritic LPSO phases exhibit an average composition (at.%) of 88.3Mg-4.0Gd-3.0Y-4.6Zn-0.1Zr as indicated by EDS. Clusters of firework shape appear in most  $\alpha$ -Mg grains, and the EDS examination reveals that slices of these clusters are averagely composed of 44.6Mg-33.6Zr-20.1Zn-1.7Y (at.%). They should be Zr clusters which acted as the grain refiner during solidification and led to a much finer  $\alpha$ -Mg ( $\sim$  54  $\mu$ m) grain size than that (millimeter level) of Mg-RE-Zn alloys without Zr content (Ref 27).

Due to the increase in Zn content, the 2# alloy exhibits several microstructural differences compared with the 1# alloy (see Fig. 2 in Ref 22). Firstly, numerous intragranular lamellar LPSO phases appear in the 2# alloy while they can be rarely observed in the 1#. It was demonstrated that the increase in Zn element in the  $\alpha$ -Mg matrix might accelerate the formation of intragranular LPSO (Ref 39, 40). Secondly, the volume fraction of interdendritic LPSO phases ( $V_{LPSO-ID}$ ) increases from 5.0 to 24.7% (about 5 times) as listed in Table 2. As a consequence, both the length and width of interdendritic LPSO phases in the 2# alloy increase. Since the width increases more than length, a lower aspect ratio (length/width) can be achieved in the 2# alloy, which explains why the interdendritic LPSO phases in the 2# alloy just occupy about twice as many grain boundaries as those in the 1# alloy do (79.1 vs. 40.0%).

### 3.2 Compression Behavior of the 2# Homogenized Alloy

The true stress-strain curves of the 2# alloy under different compression conditions are shown in Fig. 2, accompanied by the macrograph of each sample. Most curves experience the typical three stages with the increase in compression strain, including work hardening, flow softening, and dynamic stationary. However, premature fracture can be detected at the curves of 350 °C - 1/0.1 s<sup>-1</sup>, keeping in accordance with the macrocracks detected in the corresponding macrographs. Actually, besides the abovementioned parameters, all parameters with strain rate  $\dot{\epsilon} \geq 0.01$  s<sup>-1</sup> induce the obvious macrocracks on the surface of the compression samples, whether the curve is terminated prematurely or not. It preliminarily reflects the deteriorated workability of the 2# alloy compared with the 1#, since the latter just showed macrocracks at 350-450 °C and 1 s<sup>-1</sup>/350 °C and 0.1 s<sup>-1</sup>. It should be noted that the compression stress of the 2# alloy is

**Table 1 Actual composition (wt.%) of the 1# and 2# ingots**

Ingot	Nominal composition	Gd	Y	Zn	Zr	Mg	Ref
1#	Mg-5Gd-3Y-1Zn-0.5Zr	4.9	3.2	1.1	0.5	Bal	(Ref 22)
2#	Mg-5Gd-3Y-2Zn-0.5Zr	5.0	3.1	2.1	0.5	Bal	This work

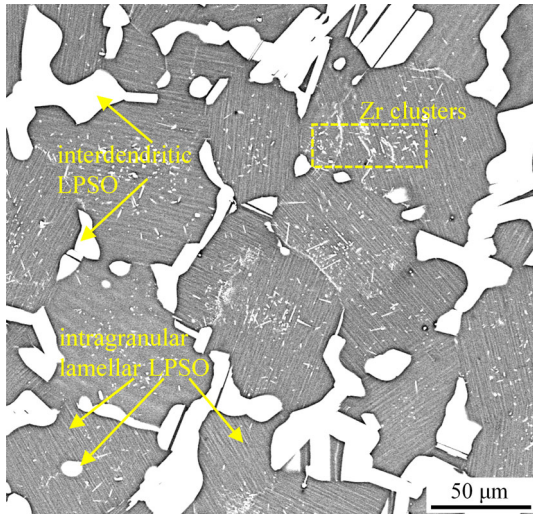


**Fig. 1** SEM image of the homogenized Mg-5.0Gd-3.1Y-2.1Zn-0.5Zr (2#) alloy

generally lower than that of the 1# alloy under the same compression conditions. The increased volume fraction of LPSO phases in the 2# failed to rise up the stress level. It probably resulted from (1) the decreased aspect ratio (length/width) of LPSO phases which determined the reinforcing effect (Ref 41) and (2) the larger DRXed grain size as shown subsequently.

To further evaluate the workability, activation energy  $Q$  and DMM processing maps need to be calculated. With the same method as for the 1# alloy (Ref 22), some important parameters of the Arrhenius equation ( $\dot{\epsilon} = A[\sinh(\alpha\sigma)]^n \cdot \exp(-\frac{Q}{RT})$ ) for the 2# alloy can be calculated according to the mean value of all slopes in Fig. 3. Therein, the average slope in Fig. 3(a) equals to  $n$  ( $= 11.3724$ ), and that in Fig. 3b equals to  $\beta$  ( $= 0.1187$ ). Thus,  $\alpha = \beta/n = 0.0104 \text{ MPa}^{-1}$ . The average slope in Fig. 3(c) and (d) (designated as  $N$  and  $S$ , respectively) is 8.12 and 4.97, respectively. Thus, the activation energy is calculated to be  $\sim 336 \text{ kJ/mol}$ , by  $Q = R \cdot N \cdot S$ . Then, the Zener–Hollomon (Z-H) parameter can be described as  $Z = \dot{\epsilon} \cdot \exp(3.36 \times 10^5/RT)$ .

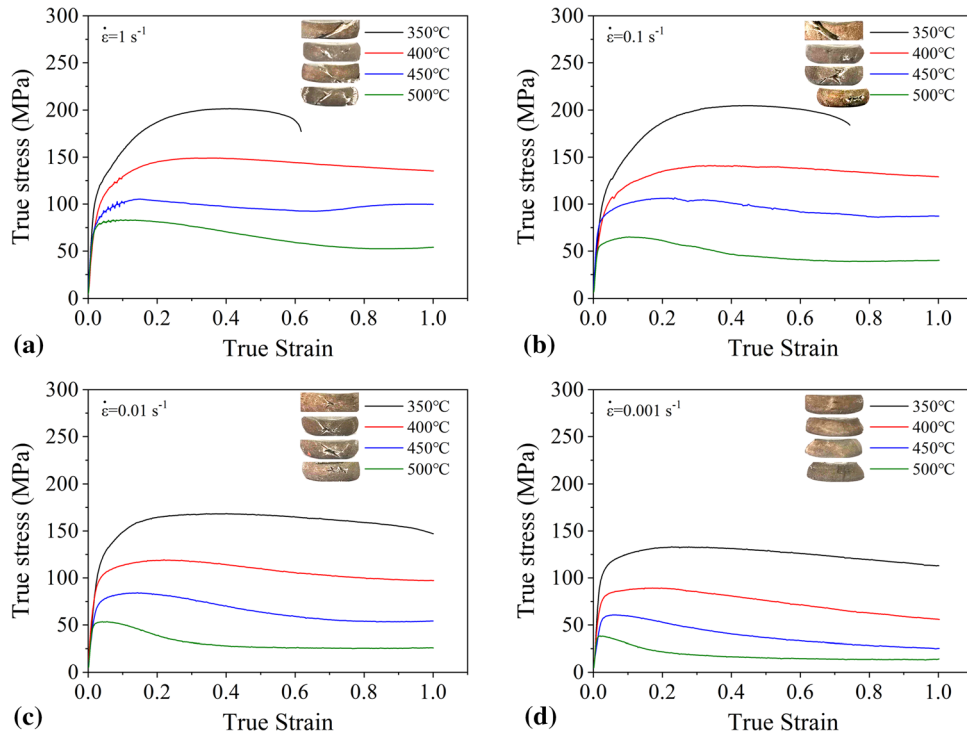


**Fig. 2** True stress–true strain curves of the 2# samples compressed at strain rates  $\dot{\epsilon}$  of (a)  $1 \text{ s}^{-1}$ , (b)  $0.1 \text{ s}^{-1}$ , (c)  $0.01 \text{ s}^{-1}$ , (d)  $0.001 \text{ s}^{-1}$ , with the insertion of their macrographs

**Table 2** Parameters about the interdendritic LPSO phases in the 1# and 2# alloys after homogenization, including the average length, width, aspect ratio, volume fraction ( $VF_{LPSO-ID}$ ), and the proportion of  $\alpha$ -Mg grain boundaries ( $P_{GB}$ ) that the interdendritic LPSO phases occupy

Sample	Length, $\mu\text{m}$	Width, $\mu\text{m}$	Aspect ratio	$VF_{LPSO-ID}$	$P_{GB}$	Ref
1#	27.2	8.7	3.1	5.0%	40.0%	(Ref 22)
2#	36.3	14.9	2.4	24.7%	79.1%	This work

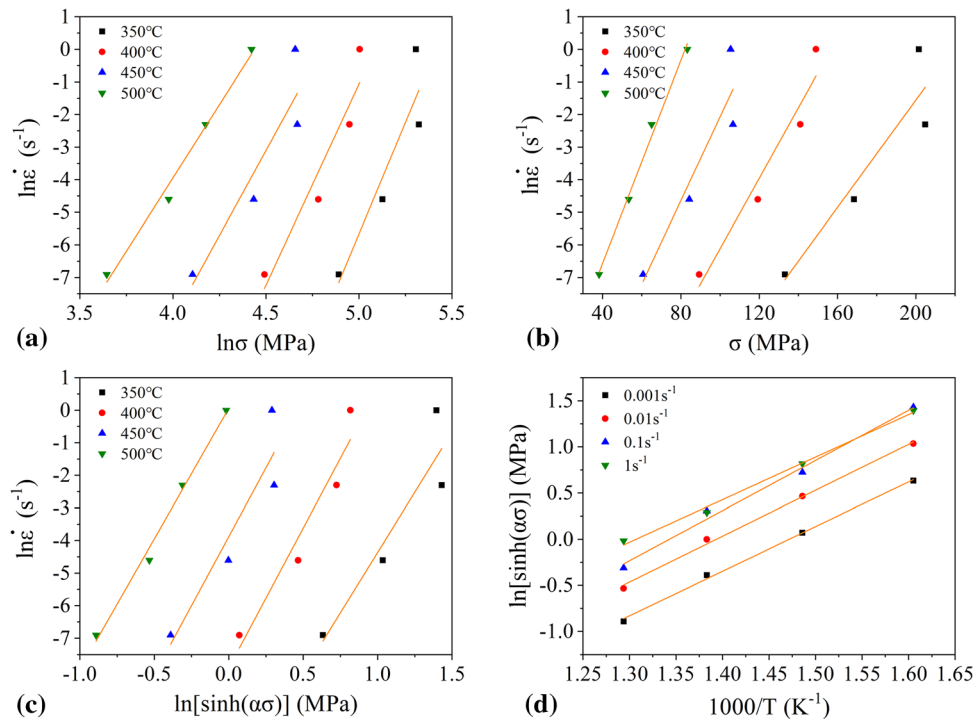


**Fig. 3** Relationship of (a)  $\ln \dot{\epsilon}$ - $\ln \sigma$ , (b)  $\ln \dot{\epsilon}$ - $\sigma$ , (c)  $\ln$ - $\ln[\sinh(\alpha\sigma)]$ , and (d)  $\ln[\sinh(\alpha\sigma)]$ - $1000/T$

### 3.3 Microstructural Evolution during Compression

Figure 4 shows the SEM images of the 2# compressed samples. Similar to the 1# alloys, the DRXed grain size and DRX ratio (the proportion of DRXed grains in  $\alpha$ -Mg matrix) increase with the increase in deformation temperature and decrease in strain rate (i.e., decrease in  $Z$ ). Both the interdendritic and intragranular LPSO phases tend to align perpendicular to the compression direction. At the lower temperatures ( $\leq 450$  °C), typical bimodal structure appears, with the DRXed grain 'necklace' surrounding the coarse deformed grains where the kinking deformation occasionally occurs.

Besides, the 2# compressed samples exhibit the following different microstructural characteristics compared with the 1# ones. Firstly, the DRX ratio of the 2# samples is lower than that of the 1# under all compression conditions, keeping in accordance with the larger  $Q$  value (336 vs. 285 kJ/mol) of the former. Secondly, there are more intragranular LPSO phases in the 2# samples. Actually, these phases already existed at the homogenized state (Fig. 1). And unlike the 1# samples, the sufficient DRX behavior at 500 °C fails to obviously dissolve intragranular LPSO phases, which indicates that the thermostability of these phases increases with the increase in Zn content. Moreover, at the majority of Z-H parameters, the grain size of the 2# samples is lower than that of the 1#. This phenomenon can be seen more intuitively in Fig. 5 which exhibits the variation in DRXed grain size as a function of  $\ln Z$ .

For both the 1# and 2# alloys, the size of DRXed grains decreases as the  $\ln Z$  increases. The relation between DRXed grain size and Z-H parameter can be described by  $Z \cdot d_{DRX}^m = C$  (Ref 42). Therein,  $d_{DRX}$  means the DRXed grain size,  $m$  is the grain size exponent, and  $C$  is a constant. The results of the 2# samples present a fitted curve with a quality ( $R^2$ ) of 0.86, and the  $m$  value is estimated as  $\sim 5.4$  with the  $C$  value equalling to  $\sim 2.17 \times 10^{25}$ .

Inverse pole figure (IPF) maps of some representative 2# samples are exhibited in Fig. 6. Except for the sample compressed at 500 °C and  $0.1 \text{ s}^{-1}$  which shows sufficient DRX, the other samples present the typical bimodal microstructure with colorful fine grains surrounding the coarse grains (generally in blue or green). According to the color designation at the lower left corner of Fig. 6(a), the fine grains own relatively randomized orientation compared with the coarse ones. In order to distinguish the DRXed and deformed grains more rigorously, the grain orientation spread (GOS) was applied and the grains with GOS less than  $2^\circ$  were considered as the DRXed ones. Among all the samples compressed at 450 °C, the strain rate of  $0.01 \text{ s}^{-1}$  induces a higher DRX ratio of 41.2% compared with the strain rate of  $0.1 \text{ s}^{-1}$  (18.1%), since a lower strain rate may favorably induce DRX like the higher temperature does (compare Fig. 6(c) with Fig. 6(d)). However, the sample compressed at 450 °C and  $0.001 \text{ s}^{-1}$  exhibits the opposite trend whose DRX ratio (17.7%) is much lower than that of  $0.01 \text{ s}^{-1}$  (41.2%).

Similar phenomenon was also observed in the 1# samples (Ref 22). Fine DRXed grains may be generated at the early stage, while they could absorb sufficient dislocations during the subsequent prolonged deformation and therefore are distinguished as deformed grains by the EBSD software. Nevertheless, the relationship between texture intensity and compression parameters is not disturbed, as shown in the corresponding pole figures (Fig. 7). Almost all these samples own the basal texture type, and the intensity increases with the increase in strain rate or decrease in temperature.

### 3.4 DMM Processing Maps of the 2# Alloy

Figure 8 shows the DMM processing maps of the 2# alloy which are made by superimposing the power dissipation maps over the instability maps, using the same calculation methods



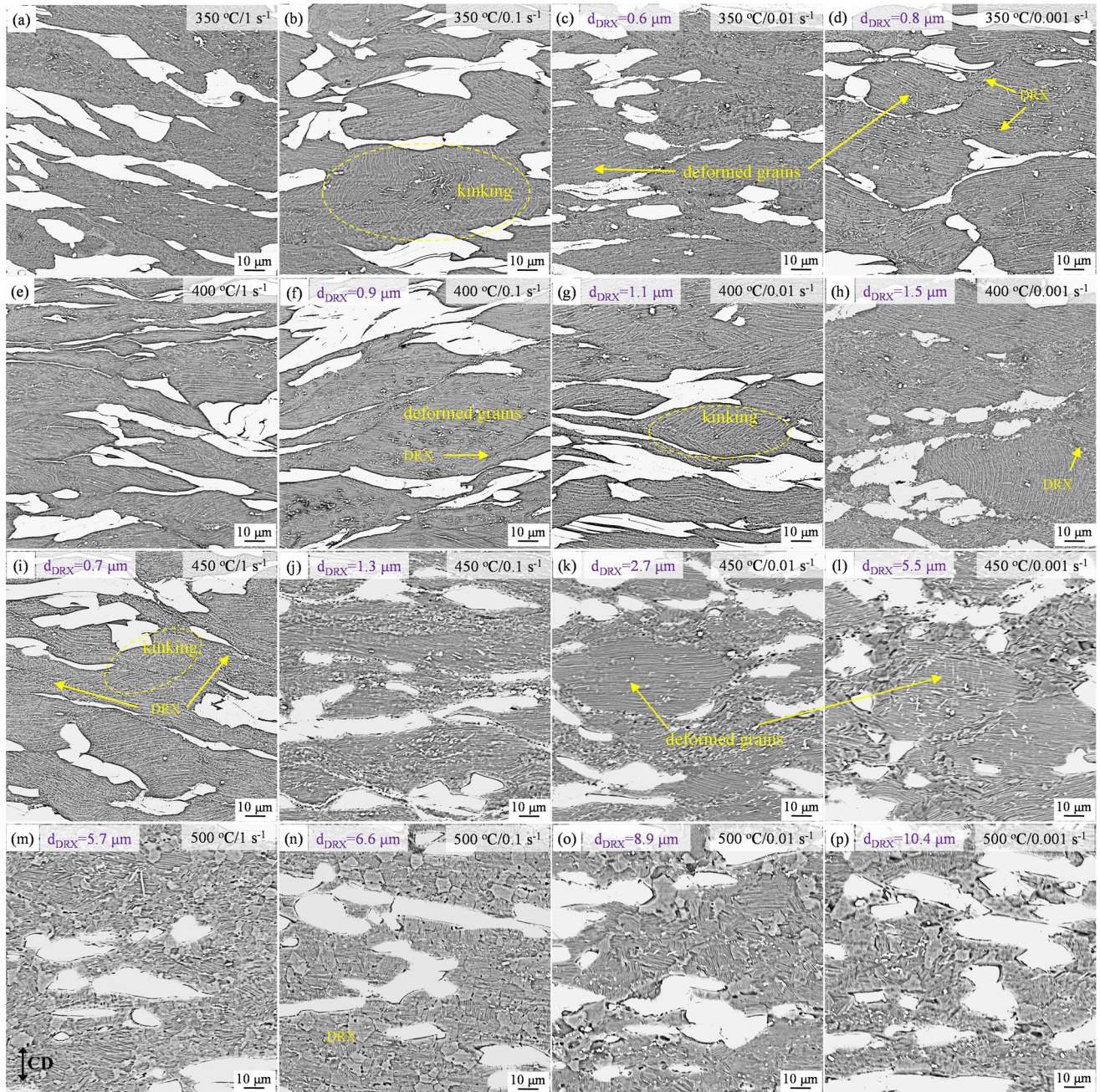


**Fig. 4** SEM images of the 2# samples compressed under different conditions

for the 1# alloy (Ref 22). To facilitate comparison, the graphs with the strain of 0.2 and 0.5 were drawn as same as 1# alloy.

At the strain of 0.2 (Fig. 8a), the efficiency larger than 32% is located in the region marked by green at the lower right corner (i.e., the region with a low  $Z$  value), but this green area is much smaller than that of the 1# alloy. Moreover, the instable region (in gray) occupies most of the area in Fig. 8(a), indicating the narrower suitable deformation condition for the 2# alloy. When the strain is increased to 0.5, the high efficiency remains in the region with a low  $Z$  value and the instable region becomes smaller, but the lower maximum efficiency (0.34 vs. 0.51) and larger gray region compared with the 1# alloy still reveal the inferior workability of the 2# alloy. At the strain of

0.5, the appropriate deformation condition lies in 430-500 °C and 0.001-0.01  $s^{-1}$ .

## 4. Discussion

### 4.1 Effect of Zn Content on $Q$ Value and Workability

The activation energy ( $Q$ ) of the 1# alloy has been compared with other commercial Mg-Al-Zn/Mg-Zn-Zr series alloys and Mg-RE-Zn alloys in our previous paper (Ref 22). It has been concluded that the moderate  $Q$  value (285 kJ/mol) of the 1# alloy mainly results from the RE atoms and interdendritic



LPSO phases. Therein, RE atoms increase the  $Q$  value via the solute drag effect which pins the movement of dislocations and grain boundaries (Ref 43). Although both the interdendritic and intragranular LPSO phases increase the  $Q$  value (Ref 24, 25, 28, 43), the thin-platelet or lamellar intragranular LPSO phases should play a bigger role since they strongly inhibit DRX while the interdendritic ones could enhance DRX to some extent through the PSN (particle simulated nucleation) mechanism (Ref 32).

In the present work, the increased Zn content in the 2# alloy mainly induces the increase in volume fraction of LPSO phases (both interdendritic and intragranular), which consume the RE atoms in  $\alpha$ -Mg matrix. The reduced RE atoms in  $\alpha$ -Mg matrix could decrease the  $Q$  value to some extent because of the reduced solute drag effect. However, the increased volume

fraction of LPSO phases, especially the lamellar intragranular ones could significantly increase the  $Q$  value and deteriorate the workability. Consequently, a higher  $Q$  value (336 kJ/mol) and inferior workability were obtained for the 2# alloy due to the increase in Zn content.

It should be mentioned that increasing the element for forming LPSO phases did not always lead to an increase in the  $Q$  value. For instance, the volume fraction of LPSO phases was tailored by changing the total content of solute atoms in Mg-Y<sub>2x</sub>-Zn<sub>x</sub> ( $x = 1, 0.5, 0.25$  at.%) alloys in our previous work (Ref 27). Unlike the present paper, the increased RE and Zn atoms hardly changed the quantity of intragranular lamellar LPSO but increased the intragranular block LPSO phases. The increased block LPSO phases could promote DRX via PSN mechanism due to their large size ( $> 1 \mu\text{m}$ ) once DRX expanded inwards the grain interior, which reduced the  $Q$  value and improved the workability (Ref 27).

The abovementioned difference might be derived from the addition of Zr element which significantly refines the initial average grain size of the 1# (36  $\mu\text{m}$ ) and 2# (54  $\mu\text{m}$ ) alloys compared with the Mg-Y<sub>2x</sub>-Zn<sub>x</sub> ( $x = 1, 0.5, 0.25$  at.%) ones (millimeter level), providing more sites for the nucleation of interdendritic LPSO phases. As a consequence, lamellar LPSO phases, which are ubiquitous in the Mg-Y<sub>2x</sub>-Zn<sub>x</sub> alloys, barely appear in the Mg-5Gd-3Y-1Zn-0.5Zr (1#) alloy. Further addition of Zn element causes a simultaneous increase in the volume fraction of interdendritic and intragranular LPSO phases in the 2# alloy. These lamellar intragranular LPSO phases instead of block ones should increase the  $Q$  value and deteriorate the workability.

From the point of view of promoting DRX, increased volume fraction of interdendritic LPSO phases seems beneficial to the workability due to the PSN mechanism as same as the intragranular block ones. However, according to Fig. 1 and

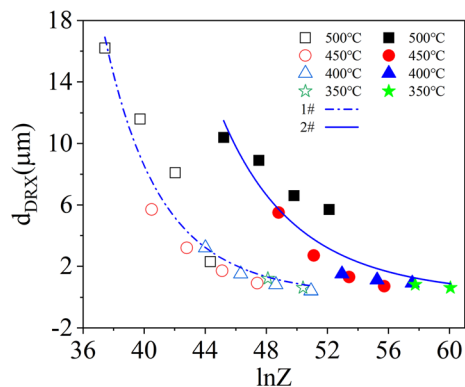


**Fig. 5** The sizes of DRXed grains plotted as a function of  $\ln Z$  for 1# and 2# alloys

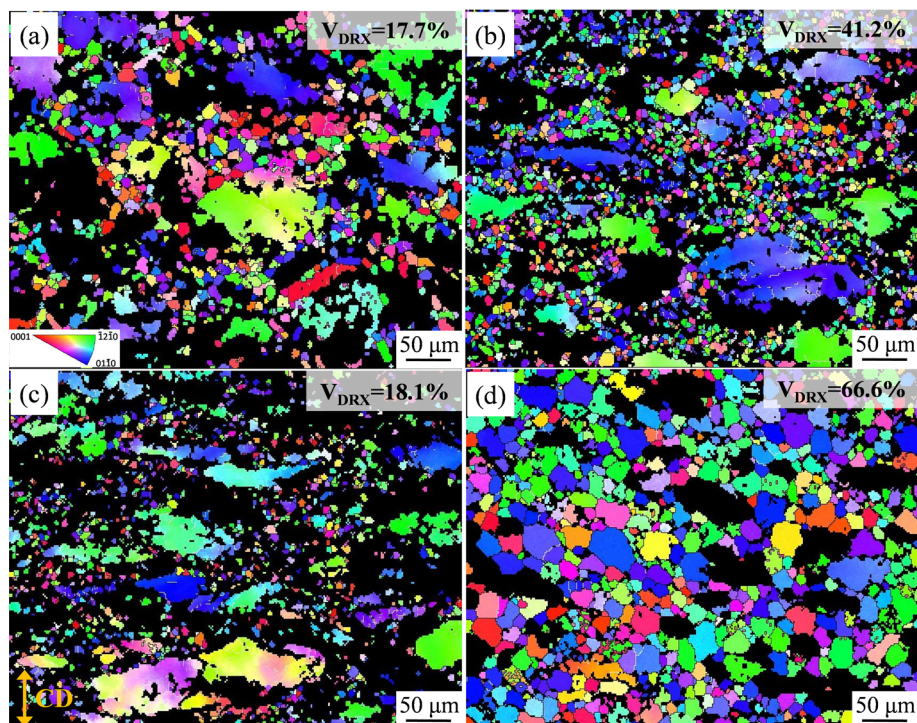


**Fig. 6** IPF maps of the 2# compressed samples under different conditions: (a) 450 °C and 0.001 s<sup>-1</sup>, (b) 450 °C and 0.01 s<sup>-1</sup>, (c) 450 °C and 0.1 s<sup>-1</sup>, and (d) 500 °C and 0.1 s<sup>-1</sup>

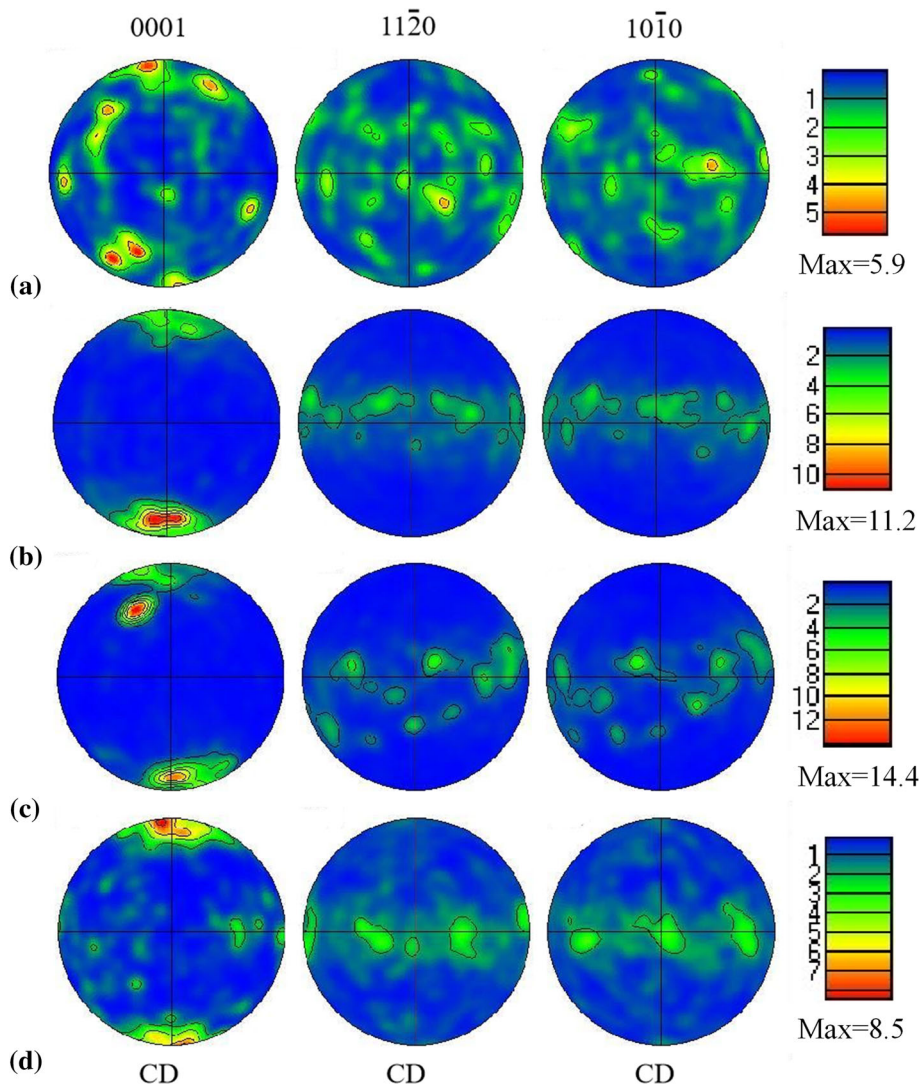


**Fig. 7** EBSD-derived pole figures of the compressed samples under different conditions: (a) 450 °C, 0.001 s<sup>-1</sup>, (b) 450 °C, 0.01 s<sup>-1</sup>, (c) 450 °C, 0.1 s<sup>-1</sup>, and (d) 500 °C, 0.1 s<sup>-1</sup>

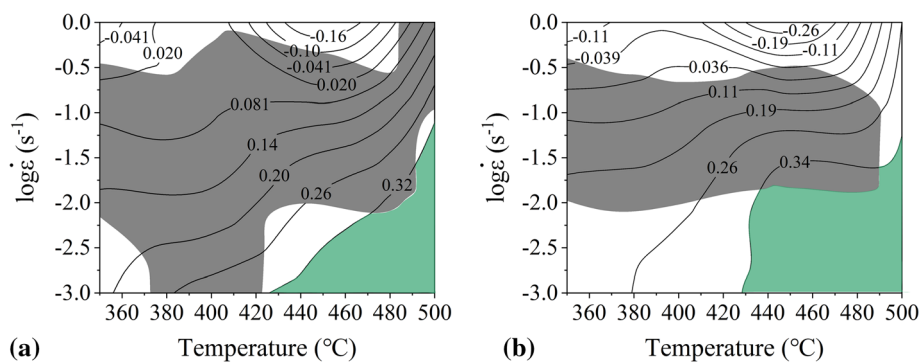


**Fig. 8** DMM processing maps at the strain of (a)  $\epsilon = 0.2$ , and (b)  $\epsilon = 0.5$  of the 2# alloy

Table 2, the width of interdendritic phases increases more than length; therefore, the increment of PSN effect should be limited. Moreover, the locations of these phases, i.e., grain boundaries, are themselves favorable nucleation sites for DRX. Once the DRX region invades the grain interior, the interdendritic LPSO might not work like the intragranular block ones

do. The improvement of workability caused by the PSN mechanism may not compensate for the decline of workability due to the back stress provided by the interdendritic LPSO (Ref 28). It follows that the changes in  $Q$  value and workability cannot be judged simply by the variation of Zn content, but by detailed changes in the LPSO morphology.



## 4.2 Comparison on DRX Behavior of Both Alloys

The variation range of the measured DRXed grain size with  $Z$  value for the 2# samples (0.6–10.4  $\mu\text{m}$ ) is smaller than that for the 1# samples (0.4–16.2  $\mu\text{m}$ ). Actually, at the majority of Z-H parameters, the average DRXed grain sizes of the 2# samples are smaller than those of the 1# ones. Such phenomenon should be attributed to the LPSO-related DRX behavior.

At the high  $Z$  value, only a few DRXed grains appear at the initial grain boundaries (I-GBs) or around interdendritic LPSO phases to form the typical bimodal microstructures. In this case, increased interdendritic LPSO phases promote the DRX nucleation due to the improved PSN effect, and meanwhile, intragranular lamellar LPSO phases could inhibit the growth and penetration of these DRXed ‘necklace’ (Ref 27, 32). As a consequence, both the finer grain sizes and lower DRX ratios are achieved compared with the 1# samples.

At the low  $Z$  value (especially at 500 °C and 0.001–0.1  $\text{s}^{-1}$ ), when DRX becomes more sufficient and invades into the grain interior, intragranular lamellar LPSO phases in 2# samples (inherited from the homogenized state) are just crushed by DRX but not dissolved into the matrix. These phases should act as the ‘skeletons’ of the DRXed grains and inhibit the migration of neighboring DRXed grain boundaries (Ref 44). Therefore, the grain growth should be suppressed compared with the corresponding 1# samples whose intragranular LPSO phases are less thermostable and dissolved into  $\alpha$ -Mg matrix during dynamic recrystallization. Moreover, under this condition, increased interdendritic LPSO may also help impede the movement of DRXed grain boundaries. Finally, the reduced variation range of DRXed grain size with  $Z$  value endows the 2# alloy with a larger grain size exponent  $m$  (5.4 vs. 4.0) than that of the 1#.

It was demonstrated that the volume fraction of LPSO phases should be an essential factor to affect the  $m$  value, since it strongly influences the DRX behavior including nucleation and growth. The 1# alloy with the  $VF_{LPSO-ID}$  of 5.0% exhibits the same  $m$  value (4.0) as the previously reported Mg-3.2Y-1.1Zn alloy who owns an approaching  $VF_{LPSO-ID}$  (6.8%) (Ref 27). As a matter of course, the  $m$  value of the 2# alloy (5.4) is larger than that of the Mg-6.7Y-2.6Zn alloy (5.0 (Ref 27)) due to the combined effects of a larger  $VF_{LPSO-ID}$  (24.7% v. 16.5%) and the more thermostable intragranular LPSO phases.

## 5. Conclusions

The compression behavior and workability of the Mg-5Gd-3Y-2Zn-0.5Zr (2#) alloy were investigated and compared with those of the Mg-5Gd-3Y-1Zn-0.5Zr (1#) one. The main conclusions are presented as follows:

- (1) Increased Zn content from 1 to 2 (wt.%) for the Mg-5Gd-3Y-xZn-0.5Zr alloys induces the increase in volume fraction and decrease in aspect ratio (length/width) of the interdendritic LPSO phases, as well as the formation of thermostable intragranular lamellar LPSO phases which appear after homogenization and keep undissolved during DRX.
- (2) Because of the increased volume fraction of LPSO phases, especially the intragranular lamellar ones which

inhibit DRX, the 2# alloy owns a higher activation energy of deformation ( $Q$ , 336 kJ/mol) compared with the 1# (285 kJ/mol). Besides the larger  $Q$  value, the deteriorated workability of the 2# alloy is also embodied in the lower efficiency of power dissipation, wider instable processing domains, and higher frequency of macrocracks in the compression samples.

- (3) At the majority of Z-H parameters ( $Z$ ), the average DRXed grain sizes and DRX ratios of the 2# samples are smaller than those of the 1#. Although increased interdendritic LPSO phases can promote DRX nucleation, increased thermostable intragranular lamellar ones strongly inhibit the DRX growth, especially at the low  $Z$  value. The increased Zn content induces the higher grain size exponent ( $m$ ,  $\sim 5.4$ ) for the 2# alloy due to the combined effects of increased interdendritic and intragranular LPSO phases.

## Acknowledgements

This work was supported by the National Natural Science Foundation of China (Nos. 51904036, 52105140 and 52174362), the Natural Science Foundation of Hunan Province (Nos. 2020JJ5600, 2021JJ30719 and 2021JJ40583), the Scientific Research Project of Hunan Education Department (Nos. 20C0088 and 21B0311), and the Changsha Municipal Natural Science Foundation (No. kq2014095).

## References

1. Y. Wan, B. Tang, Y. Gao, L. Tang, G. Sha, B. Zhang, N. Liang, C. Liu, S. Jiang, Z. Chen, X. Guo, and Y. Zhao, Bulk Nanocrystalline High-Strength Magnesium Alloys Prepared via Rotary Swaging, *Acta Mater.*, 2020, **200**, p 274–286
2. X. Chen, C. Liu, M. Fang, S. Jiang, Z. Chen, and Y. Wan, Strengthening the Mg-Y-Zn Alloy through the Formation of Nanoscale Lamellar Structures and Nanograins, *J. Alloy. Compd.*, 2021, **886**, p 161148
3. B. Zhu, X. Liu, C. Xie, J. Su, P. Guo, C. Tang, and W. Liu, Unveiling the Underlying Mechanism of Forming Edge Cracks Upon High Strain-Rate Rolling of Magnesium Alloy, *J. Mater. Sci. Technol.*, 2020, **50**, p 59–65
4. C. Xie, J.M. He, B.W. Zhu, X. Liu, J. Zhang, X.F. Wang, X.D. Shu, and Q.H. Fang, Transition of Dynamic Recrystallization Mechanisms of As-Cast AZ31 Mg Alloys during Hot Compression, *Int. J. Plast.*, 2018, **111**, p 211–233
5. H. Liu, H. Huang, C. Wang, J. Sun, J. Bai, F. Xue, A. Ma, and X.-B. Chen, Recent Advances in LPSO-Containing Wrought Magnesium Alloys: Relationships Between Processing, Microstructure, and Mechanical Properties, *JOM*, 2019, **71**(9), p 3314–3327
6. M. Fang, C. Liu, S. Jiang, H. Xiao, G. Zeng, X. Chen, and Y. Wan, Nanocrystallization of Mg-Y-Zn Alloy Containing long-Period Stacking-Ordered Phase during Cold Rotary Swaging, *J. Mater. Eng. Perform.*, 2022 <https://doi.org/10.1007/s11665-021-06549-8>
7. X. Yuan, Y. Du, D. Dong, D. Liu, and B. Jiang, Corrosion Resistance Improvement of an Extruded Mg-Gd-Y-Zn-Zr-Ca via Aging Treatment, *J. Mater. Eng. Perform.*, 2021, **31**(4), p 2909–2917
8. W. Huang, J. Chen, R. Zhang, X. Yang, L. Jiang, Z. Xiao, and Y. Liu, Effect of Deformation Modes on Continuous Dynamic Recrystallization of Extruded AZ31 Mg Alloy, *J. Alloy. Compd.*, 2022, **897**, p 163086
9. W. Huang, H. Huang, W. Li, J. Chen, S. Zhang, and Z. Xiao, Influence of Heat Treatment and Pre-straining on Dynamic Precipitation and Creep Behavior of AZ91-0.5Y Magnesium Alloys, *Mater. Sci. Eng. A*, 2022, **841**, p 143049



10. P. Sekar and N.S.V. Desai, Recent Progress in in vivo Studies and Clinical Applications of Magnesium Based Biodegradable Implants—A Review, *J. Magnes. Alloy.*, 2021, 9(4), p 1147–1163
11. T. Long, X. Zhang, Q. Huang, L. Liu, Y. Liu, J. Ren, Y. Yin, D. Wu, and H. Wu, Novel Mg-Based Alloys by Selective Laser Melting for Biomedical Applications: Microstructure Evolution, Microhardness and in vitro Degradation Behaviour, *Virtual Phys. Prototyp.*, 2017, 13(2), p 71–81
12. Y. Yin, Q. Huang, L. Liang, X. Hu, T. Liu, Y. Weng, T. Long, Y. Liu, Q. Li, S. Zhou, and H. Wu, In vitro Degradation Behavior and Cytocompatibility of ZK30/Bioactive Glass Composites Fabricated by Selective Laser Melting for Biomedical Applications, *J. Alloy. Compd.*, 2019, 785, p 38–45
13. Y. Yang, X. Xiong, J. Chen, X. Peng, D. Chen, and F. Pan, Research Advances in Magnesium and Magnesium Alloys Worldwide in 2020, *J. Magnes. Alloy.*, 2021, 9(3), p 705–747
14. N.A. Ali and M. Ismail, Advanced Hydrogen Storage of the Mg-Na-Al System: A Review, *J. Magnes. Alloy.*, 2021, 9(4), p 1111–1122
15. J.H. He, J. Zhang, X.J. Zhou, J.N. Chen, L.P. Yu, L.K. Jiang, X.Z. Lu, X.M. Chen, and D.W. Zhou, Hydrogen Storage Properties of Mg<sub>98.5</sub>Gd<sub>1</sub>Zn<sub>0.5</sub> and Mg<sub>98.5</sub>Gd<sub>0.5</sub>Y<sub>0.5</sub>Zn<sub>0.5</sub> Alloys Containing LPSO Phases, *Int J Hydrogen Energy*, 2021, 46(65), p 32949–32961. <https://doi.org/10.1016/j.ijhydene.2021.07.140>
16. J.N. Chen, J. Zhang, J.H. He, X.J. Zhou, X.Z. Lu, X.M. Chen, L.P. Yu, and D.W. Zhou, A Comparative Study on Hydrogen Storage Properties of as-Cast and Extruded Mg-4.7Y-4.1Nd-0.5Zr Alloys, *J. Phys. Chem. Solids*, 2022, 161, p 110483
17. C. Xu, M.Y. Zheng, S.W. Xu, K. Wu, E.D. Wang, S. Kamado, G.J. Wang, and X.Y. Lv, Ultra High-Strength Mg-Gd-Y-Zn-Zr Alloy Sheets Processed by Large-Strain Hot Rolling and Ageing, *Mater. Sci. Eng. A*, 2021, 547, p 93–98
18. W.T. Sun, X.G. Qiao, M.Y. Zheng, X.J. Zhao, H.W. Chen, N. Gao, and M.J. Starink, Achieving Ultra-High Hardness of Nanostructured Mg-8.2Gd-3.2Y-1.0Zn-0.4Zr alloy Produced by a Combination of High Pressure Torsion and Ageing Treatment, *Scripta Mater.*, 2018, 155, p 21–25
19. W.T. Sun, X.G. Qiao, M.Y. Zheng, C. Xu, S. Kamado, X.J. Zhao, H.W. Chen, N. Gao, and M.J. Starink, Altered Ageing Behaviour of a Nanostructured Mg-8.2Gd-3.8Y-1.0Zn-0.4Zr Alloy Processed by High Pressure Torsion, *Acta Mater.*, 2018, 151, p 260–270
20. J. Zheng, Z. Chen, Z. Yan, Z. Zhang, Q. Wang, and Y. Xue, Preparation of Ultra-High Strength Mg-Gd-Y-Zn-Zr Alloy by Pre-ageing Treatment Prior to Extrusion, *J. Alloy. Compd.*, 2022, 894, p 162490
21. J. Zheng, Z. Chen, Z. Yan, Z. Zhang, and Y. Xue, An Alternating ageing-Annealing Process for Enhancing Strength and Ductility of a Mg-Gd-Y-Zn-Zr Alloy, *Mater. Sci. Eng. A*, 2021, 828, p 142103
22. X. Zhou, Y. Yao, J. Zhang, X. Chen, W. Huang, J. Pan, H. Wang, and M. Weng, A High-Performance Mg-4.9Gd-3.2Y-1.1Zn-0.5Zr Alloy via Multidirectional Forging After Analyzing its Compression Behavior, *J. Mater. Sci. Technol.*, 2021, 70, p 156–167
23. X. Zhou, W. Xiong, G. Zeng, H. Xiao, J. Zhang, X. Lu, and X. Chen, Combined Effects of LPSO Orientation and  $\alpha$ -Mg Texture on Tensile Anisotropy of an Extruded Mg-Gd-Y-Zn-Zr alloy, *Mater. Sci. Eng. A*, 2021, 805, p 140596
24. B.-J. Lv, J. Peng, Y. Peng, A.-T. Tang, and F.-S. Pan, The Effect of LPSO Phase on Hot Deformation Behavior and Dynamic Recrystallization Evolution of Mg-2.0Zn-0.3Zr-5.8Y Alloy, *Mater. Sci. Eng. A*, 2013, 579(5), p 209–216
25. B.-J. Lv, J. Peng, L.-L. Zhu, Y.-J. Wang, and A.-T. Tang, The Effect of 14H LPSO Phase on Dynamic Recrystallization Behavior and Hot Workability of Mg-2.0Zn-0.3Zr-5.8Y Alloy, *Mater. Sci. Eng. A*, 2014, 599, p 150–159
26. Y. Li, W. Xiao, F. Wang, T. Hu, and C. Ma, The Roles of Long Period Stacking Ordered Structure and Zn Solute in the Hot Deformation Behavior of Mg-Gd-Zn Alloys, *J. Alloy. Compd.*, 2018, 745, p 33–43
27. X. Zhou, Y. Yao, J. Zhang, X. Lu, K. Xu, H. Liu, and Z. Wu, Improved Workability for Mg-Y-Zn Alloys via Increased Volume Fraction of block LPSO Phases, *Mater. Sci. Eng. A*, 2020, 794, p 139934
28. X. Zhou, C. Liu, Y. Gao, S. Jiang, W. Liu, and L. Lu, Hot Compression Behavior of the Mg-Gd-Y-Zn-Zr Alloy Filled With Intragranular Long-Period Stacking Ordered Phases, *J. Alloy. Compd.*, 2017, 724, p 528–536
29. X. Zhou, C. Liu, Y. Gao, S. Jiang, and Z. Chen, Improved Workability and Ductility of the Mg-Gd-Y-Zn-Zr Alloy via Enhanced Kinking and Dynamic Recrystallization, *J. Alloy. Compd.*, 2018, 749, p 878–886
30. Y.M. Zhu, A.J. Morton, and J.F. Nie, The 18R and 14H Long-Period Stacking Ordered Structures in Mg-Y-Zn Alloys, *Acta Mater.*, 2010, 58(8), p 2936–2947
31. Y.M. Zhu, A.J. Morton, and J.F. Nie, Growth and Transformation Mechanisms of 18R and 14H in Mg-Y-Zn Alloys, *Acta Mater.*, 2012, 60(19), p 6562–6572
32. X. Zhou, C. Liu, Y. Gao, S. Jiang, X. Han, and Z. Chen, Evolution of LPSO Phases and their Effect on Dynamic Recrystallization in a Mg-Gd-Y-Zn-Zr Alloy, *Metall. Mater. Trans. A*, 2017, 48(6), p 3060–3072
33. L. Zheng, C. Liu, J. Jin, X. Wang, and D. Ji, Effect of Hot-Rolling on Microstructures and Mechanical Properties of Extruded Mg-6Gd-3.2Y-xZn-0.5Zr Sheet, *J. Mater. Eng. Perform.*, 2012, 22(1), p 104–111. <https://doi.org/10.1007/s11665-012-0238-8>
34. M. Suzuki, T. Kimura, J. Koike, and K. Maruyama, Effects of Zinc on Creep Strength and Deformation Substructures in Mg-Y alloy, *Mater. Sci. Eng. A*, 2004, 387–389, p 706–709
35. M. Suzuki, T. Kimura, J. Koike, and K. Maruyama, Strengthening Effect of Zn in Heat Resistant Mg-Y-Zn Solid Solution Alloys, *Scripta Mater.*, 2003, 48(8), p 997–1002
36. Z. Yu, C. Xu, J. Meng, X. Zhang, and S. Kamado, Microstructure Evolution and Mechanical Properties of as-Extruded Mg-Gd-Y-Zr Alloy with Zn and Nd Additions, *Mater. Sci. Eng. A*, 2018, 713, p 234–243
37. Y. Zhou, P. Fu, L. Peng, D. Wang, Y. Wang, B. Hu, M. Liu, A.K. Sachdev, and W. Ding, Precipitation Modification in Cast Mg-1Nd-1Ce-Zr Alloy by Zn Addition, *J. Magnes. Alloy.*, 2019, 7(1), p 113–123
38. K. Liu, J. Zhang, G. Su, L.L. Rokhlin, F.M. Elkin, and J. Meng, Influence of Zn Content on the Microstructure and Mechanical Properties of Extruded Mg-5Y-4Gd-0.4Zr alloy, *J. Alloy. Compd.*, 2009, 481(1–2), p 811–818. <https://doi.org/10.1016/j.jallcom.2009.03.119>
39. L. Liu, X. Zhou, Y. Shilun, J. Zhang, L. Xianzheng, X. Shu, and S. Zaijun, Effects of Heat Treatment on Mechanical Properties of an Extruded Mg-4.3Gd-3.2Y-1.2Zn-0.5Zr Alloy and Establishment of its Hall–Petch Relation, *J. Magnes. Alloy.*, 2022, 10(2), p 501–512. <https://doi.org/10.1016/j.jma.2020.09.023>
40. X. Zhou, C. Liu, Y. Gao, S. Jiang, and Z. Chen, Mechanical Properties of the Mg-Gd-Y-Zn-Zr Alloys with Different Morphologies of Long-Period Stacking Ordered Phases, *J. Mater. Eng. Perform.*, 2018, 27(11), p 6237–6245
41. K. Hagihara, A. Kinoshita, Y. Sugino, M. Yamasaki, Y. Kawamura, H.Y. Yasuda, and Y. Umakoshi, Effect of Long-Period Stacking Ordered Phase on Mechanical Properties of Mg<sub>97</sub>Zn<sub>1</sub>Y<sub>2</sub> Extruded Alloy, *Acta Mater.*, 2010, 58(19), p 6282–6293
42. H. Watanabe, H. Tsutsui, T. Mukai, K. Ishikawa, Y. Okanda, M. Kohzu, and K. Higashi, Grain size Control of Commercial Wrought Mg-Al-Zn Alloys Utilizing Dynamic Recrystallization, *Mater. Trans.*, 2001, 42(7), p 1200–1205
43. X. Jin, W. Xu, D. Shan, C. Liu, and Q. Zhang, Deformation Behavior, Microstructure Evolution and Hot Workability of Mg-3.7Gd-2.9Y-0.7Zn-0.7Zr alloy, *Met. Mater. Int.*, 2017, 23(3), p 434–443
44. X. Zhou, C. Liu, Y. Gao, S. Jiang, W. Liu, and L. Lu, Microstructure and Mechanical Properties of Extruded Mg-Gd-Y-Zn-Zr Alloys filled with intragranular LPSO Phases, *Mater. Charact.*, 2018, 135, p 76–83

**Publisher's Note** Springer Nature remains neutral with regard to jurisdictional claims in published maps and institutional affiliations.

Springer Nature or its licensor holds exclusive rights to this article under a publishing agreement with the author(s) or other rightsholder(s); author self-archiving of the accepted manuscript version of this article is solely governed by the terms of such publishing agreement and applicable law.